RESEARCH ARTICLE | NOVEMBER 12 2024

Bouncing dynamics of a droplet impacting onto a superhydrophobic surface with pillar arrays 🔵 ✅

Xin Wang (王鑫) 🔵 ; Mengqi Zhang (张蒙齐) 🔵 ; Hui Tang (唐辉) 🔵 ; Chenglei Wang (王成磊) ✉ 🔵

🔴 Check for updates

View Online

Export Citation

Articles You May Be Interested In

Research on the contact time of a bouncing microdroplet with lattice Boltzmann method

Physics of Fluids (April 2021)

Droplet impact dynamics on single-pillar superhydrophobic surfaces

Physics of Fluids (October 2021)

Impact force of ring bouncing on superhydrophobic surface with a bead

Physics of Fluids (May 2023)

08 December 2025 09:23:46

Bouncing dynamics of a droplet impacting onto a superhydrophobic surface with pillar arrays _{EP}

View Online   Export Citation   CrossMark

Xin Wang (王鑫),[1,2] (iD) Mengqi Zhang (张蒙齐),[3] (iD) Hui Tang (唐辉),[1] (iD) and Chenglei Wang (王成磊)[1,4,5,a] (iD)

AFFILIATIONS

[1]Department of Mechanical Engineering, The Hong Kong Polytechnic University, Hong Kong, China
[2]School of Energy and Environment, Southeast University, Nanjing, P.R. China
[3]Department of Mechanical Engineering, National University of Singapore, Singapore, Singapore
[4]Institute of High Performance Computing (IHPC), Agency for Science, Technology and Research (A*STAR), 1 Fusionopolis Way, #16-16 Connexis, Singapore 138632, Singapore
[5]The Hong Kong Polytechnic University Shenzhen Research Institute, Shenzhen 518057, PR China

[a]Author to whom correspondence should be addressed: chenglei.wang@polyu.edu.hk and wangcl1@ihpc.a-star.edu.sg

ABSTRACT

A superhydrophobic surface (SHS) patterned with pillar arrays has been demonstrated to achieve excellent water repellency and is highly effective for self-cleaning, anti-icing/frosting, etc. However, the droplet impact dynamics and the related mechanism for contact time (t_c^*) reduction remain elusive, especially when different arrangements of pillar arrays are considered. This study aims to bridge this gap by exploring a droplet impinging on an SHS with square pillar arrays in a cuboid domain. This fluid dynamics problem is numerically simulated by applying the lattice Boltzmann method. The influences of the droplet diameter (D^*), the Weber number (We_w), and the pillar spacing and height (s^* and h^*) on the droplet dynamics and t_c^* are investigated. The numerical results show that the droplet can exhibit different bouncing patterns, normal or pancake bouncing, depending on We_w, s^*, and h^*. Pancake bouncing usually occurs when $We_w \geq 1.28$, $h^* \geq 1$, and $s^* \approx 1$, yielding a small t_c^*. Among all cases, a small t_c^* can be attained when the conversion rate of kinetic energy to surface energy (ΔE_{sur}^*) right after the impacting exceeds a critical value around 0.038. This relation broadens that given in A. M. Moqaddam *et al.* [J. Fluid Mech. 824, 866–885 (2017)], which reported that the large total change of surface area renders small t_c^*. Furthermore, the maximum impacting force remains nearly the same in all cases, regardless of the bouncing patterns.

I. INTRODUCTION

Droplets impinging solid surfaces are omnipresent in nature and engineering applications, and they can exhibit complex dynamic behaviors, including spreading, bouncing, splashing, spinning, icing, and boiling.[1–5] Such behaviors are dominated by a variety of factors, such as droplet properties including size, velocity, viscosity, surface tension, temperature, surface properties encompassing temperature and morphology, wettability arising from intermolecular interactions among all phases in contact, and environmental temperature and pressure. Some of these factors can be tuned to manipulate the droplet impingement dynamics associated with contact time,[2] spreading pattern,[1,4] bouncing deformation,[2,3] etc. In many engineering systems, controlling droplet impact dynamics is important, particularly when it comes to the reduction of contact time, which is a common concern across numerous applications, including anti-icing,[6] self-cleaning,[7] inkjet printing,[8] and anti-corrosion.[9]

Contact time is referred to as the period that a droplet remains in contact with the solid surface after impacting it. Superhydrophobic surfaces (SHSs) have been extensively applied for the reduction of

contact time. Richard *et al.*[2] revealed that for droplets impacting flat SHSs, inertial effects are dominant, and the contact time is determined by the balance between inertia and capillary effects. Under this condition, the contact time increases with droplet radius but is independent of impact velocity. This sets a theoretical limit for the contact time of droplets impacting SHSs.

Recent studies revealed that when small-scale structures are incorporated into flat SHSs, the overall wettability is modified, the impingement dynamics of droplets can be altered, and shorter contact time is achievable, breaking the theoretical limit proposed by Richard *et al.*[2] In literature, two popular structures of this type are ridge structures and arrays of pillars/posts.

The efficacy of using ridge structures for contact time reduction was tested in a pioneer work by Bird *et al.*,[10] where a 37% reduction was achieved. After that, such strategies have been adopted in numerous follow-up studies and their effectiveness for contact time reduction has been widely examined.[11–15] For instance, Shen *et al.*[11] reported that "three-forked," "cross-shaped," and "five-forked" ridge structures

can further increase droplet deformation and reduce droplet contact time compared to when only one ridge structure is applied. Furthermore, ridge structures have also been applied on curved SHSs, such as cylindrical SHSs, for contact time reduction, as demonstrated in Chen *et al.*[12] and Zhang *et al.*[13] More related studies can be found in some recent comprehensive reviews.[16–18]

In the above studies, a limited number of ridges are applied. When droplets cannot directly impact them, their effectiveness in reducing contact time decreases. This disadvantage can be overcome by integrating arrays of pillars/posts on SHSs. For example, Liu *et al.*[19,20] found that pillar arrays can cause an extremely fast droplet detachment without recoiling (named as "pancake bouncing") by effectively converting the surface energy of the impinging drop into kinetic energy for the upward motion. Wang *et al.*[21] investigated the droplet impact on pillar-arrayed polydimethylsiloxane surfaces with different solid fractions. The contact time of bouncing droplets on sparse pillars was drastically shortened due to the accelerated retraction. Patil *et al.*[22] found that an intermediate pillar spacing can result in full bouncing, while other spacing can cause partial bouncing. Hu and Liu[23] investigated the dynamic characteristics of microdroplet impingement on array structured SHSs at a wide range of impacting velocities and showed that the droplet's contact time is in the range of microseconds and pillar height increased the droplet's surface adhesion. Song *et al.*[24] observed typical pancake bouncing on the superhydrophobic pillar arrays of 1.05 mm diameter, 0.8 mm height, and 0.25 mm spacing, yielding a 57.8% reduction in contact time. Wu *et al.*[25] designed a dual gradient surface consisting of a vertical spacing gradient made of tapered pillar arrays and a lateral curvature gradient characterized as macroscopic convex. The impinging droplet at low Weber number (*We*) presented an asymmetric bouncing mode with a contact time reduction of 20%, while the pancake bouncing mode at high *We* was adopted with a contact time reduction of 70%. Ma *et al.*[26] studied the bouncing dynamics of impinging droplets on the nano-pillared SHSs and explored the effects of *We*, solid fraction (fixed pillar width), and pillar height. There exists an optimal range of solid fraction and pillar height to induce pancake bouncing at intermediate *We*. The critical *We* to trigger pancake bouncing was affected largely by nanostructures. To reveal the fundamental mechanism of using SHS with pillar arrays for contact time reduction, Moqaddam *et al.*[27] investigated the dynamic behaviors of a droplet impacting on surfaces with tapered posts over a wide range of *We*, figuring out that increase in surface area allows to store kinetic energy during impingement, which in turn reduces the contact time.

Although SHSs patterned with arrays of pillars/posts have been proven effective in reducing the contact time, the mechanism for manipulating the impingement dynamics of a droplet has not been fully understood, especially when different pillar arrangements are considered. This paper aims to bridge this gap through a systematic computational study. Specifically, an SHS with arrays of square pillars of different heights and spacings is considered, and the impact dynamics of droplets of distinct sizes on such surfaces at various *We* are explored. A mechanism contributing to the reduction of contact time is elucidated through a comprehensive analysis, together with the analysis of the effects of other factors on associated properties pertinent to impact dynamics, including spreading factor, impacting force, and evolutions of kinetic, surface, and dissipation energy during impingement.

The outline of this paper is as follows: The problem and methodology are described in Sec. II. The simulation results are given in Sec.

III, where the influences of droplet size, Weber number, and pillar spacing and height on the impact dynamics are revealed, and the dominant factor for the contact time is identified. The conclusions of this work are presented in Sec. IV.

II. PROBLEM DESCRIPTION AND METHODOLOGY
A. Problem description

Figure 1 shows the model of a droplet of diameter D_0 impacting a superhydrophobic surface (SHS) patterned with an array of square pillars at an initial velocity U_0 in a cuboid domain with edge length L. The height, width, and spacing of the pillar array are h, w, and s, respectively.

B. Methodology

The impingement dynamics of the droplet is solved numerically based on the lattice Boltzmann method (LBM). The Bhatnagar–Gross–Krook collision algorithm is adopted, and the lattice Boltzmann equation is given by Chen *et al.*,[28]

$$f_\alpha(\boldsymbol{x} + \boldsymbol{e}_\alpha\delta_t, t + \delta_t) - f_\alpha(\boldsymbol{x}, t) = -\frac{1}{\tau}\left[f_\alpha(\boldsymbol{x}, t) - f_\alpha^{eq}(\boldsymbol{x}, t)\right] + \Delta f_\alpha(\boldsymbol{x}, t),$$

(1)

where $f_\alpha(\boldsymbol{x}, t)$ is the distribution function at time t and position $\boldsymbol{x}$ with velocity $\boldsymbol{e}_\alpha$. δ_t is the time step. τ denotes the relaxation time. $\Delta f_\alpha(\boldsymbol{x}, t)$ is the body force term. $f_\alpha^{eq}(\boldsymbol{x}, t)$ is the equilibrium distribution function, which can be written as

$$f_\alpha^{eq} = \omega_\alpha\rho\left[1 + \frac{\boldsymbol{e}_\alpha \cdot \boldsymbol{u}}{c_s^2} + \frac{(\boldsymbol{e}_\alpha \cdot \boldsymbol{u})^2}{2c_s^4} - \frac{\boldsymbol{u}^2}{2c_s^2}\right],$$

(2)

where ω_α is the weighting factor, c_s is the speed of sound. ρ is the fluid density, and $\boldsymbol{u}$ is the fluid velocity, which can be expressed as

$$\rho = \sum_\alpha f_\alpha(\boldsymbol{x}, t), \ \boldsymbol{u} = \frac{\sum_\alpha \boldsymbol{e}_\alpha f_\alpha(\boldsymbol{x}, t)}{\sum_\alpha f_\alpha(\boldsymbol{x}, t)}.$$

(3)

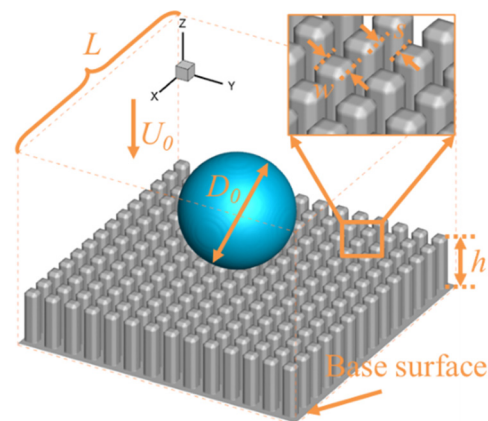The kinematic viscosity of fluid (ν) is derived from an extended multi-scale Chapman–Enskog analysis,

FIG. 1. Schematic of a droplet impacting an SHS patterned with square pillar arrays in a cuboid domain.

$$\upsilon = c_s^2(\tau - 0.5)\delta_t. \tag{4}$$

Herein, a three-dimensional LBM model, i.e., D3Q19 model, is applied. As such, $\omega_\alpha = 1/3$ for $\alpha = 0$, $\omega_\alpha = 1\sim18$ for $\alpha = 1\text{–}6$, and $\omega_\alpha = 1/36$ for $\alpha = 7\text{–}18$.[29] $c_s = c/\sqrt{3}$, where $c = \delta_x/\delta_t$, δ_x is the lattice spacing, and $\delta_t = 1$ and $\delta_x = 1$ in LBM by convention. The discrete velocity is written as

$$\mathbf{e}_\alpha = \begin{cases} (0,0,0), & \alpha = 0, \\ (\pm1,0,0)(0,\pm1,0)(0,0,\pm1), & \alpha = 1\sim6, \\ (\pm1,\pm1,0)(0,\pm1,\pm1)(\pm1,0,\pm1), & \alpha = 7\sim18. \end{cases} \tag{5}$$

The force term $\Delta f_\alpha(\mathbf{x}, t)$ is incorporated into Eq. (1) using the exact difference method,[30,33] which can avoid the physically unrealistic relaxation phenomena over a wide range of relaxation times, written as

$$\Delta f_\alpha(\mathbf{x}, t) = f_\alpha^{eq}[\rho(\mathbf{x},t), \mathbf{u} + \Delta\mathbf{u}] - f_\alpha^{eq}[\rho(\mathbf{x},t), \mathbf{u}], \tag{6}$$

where the variation of velocity $\Delta\mathbf{u}$ can be derived from

$$\Delta\mathbf{u} = \mathbf{F} \cdot \delta_t/\rho. \tag{7}$$

$\mathbf{F}$ is the total force density composed of the fluid–fluid force density ($\mathbf{F}_{int}$), the fluid–solid force density ($\mathbf{F}_s$), and the gravitational force density ($\mathbf{F}_g$). In this study, a single component multiple phase pseudopotential model is applied. According to Kupershtokh et al.[31,32] and Gong and Cheng,[33] $\mathbf{F}_{int}$ can be expressed as

$$\mathbf{F}_{int} = -\beta\psi(\mathbf{x})\sum_\alpha G(\mathbf{x},\mathbf{x}')\psi(\mathbf{x} + \mathbf{e}_\alpha\delta_t)\mathbf{e}_\alpha$$
$$- \frac{1-\beta}{2}\sum_\alpha G(\mathbf{x},\mathbf{x}')\psi^2(\mathbf{x} + \mathbf{e}_\alpha\delta_t)\mathbf{e}_\alpha, \tag{8}$$

where the value of β and $G(\mathbf{x},\mathbf{x}')$ can be found in Ref. 33. In D3Q19 model, $\psi(\mathbf{x})$ is given as

$$\psi(\mathbf{x}) = \sqrt{2(p - \rho c_s^2)/c_0 B}, \tag{9}$$

$B = -1.0$ and $c_0 = 6$,[34] and p is the pressure, which can be evaluated as

$$p = \frac{\rho R'T}{1 - b\rho} - \frac{a\rho^2\alpha(T)}{1 + 2b\rho - b^2\rho^2}. \tag{10}$$

Based on the Peng-Robinson (P-R) equation of state,[35] where $R' = 1, a = \frac{2}{49}, b = \frac{2}{21}, \alpha(T) = \left[1 + 0.87324\left(1 - \sqrt{\frac{T}{T_{cr}}}\right)\right]^2$.[33] $\mathbf{F}_s$ can be evaluated by

$$\mathbf{F}_s(\mathbf{x}) = -G_s\psi(\mathbf{x})\sum_\alpha \omega_\alpha S(\mathbf{x} + \mathbf{e}_\alpha\delta_t), \tag{11}$$

where G_s describes the strength of force between the fluid and surface and determines the wall wettability. S denotes an indicator function with $S = 1$ for solid and $S = 0$ for fluid. $\mathbf{F}_g$ can be written as

$$\mathbf{F}_g(\mathbf{x}) = (\rho - \rho_v)\mathbf{g}, \tag{12}$$

where g is the gravitational acceleration and ρ_v represents the gas density. The velocity $\mathbf{U}$ can be evaluated using the expression provided by Ginzbourg and Adler,[36]

$$\rho\mathbf{U} = \rho\mathbf{u} + 0.5\delta_t\mathbf{F}. \tag{13}$$

Half bounce-back boundary conditions[37] are adopted at the upper and bottom walls to achieve no-slip conditions, and periodic boundary conditions are applied on other surfaces of the domain.

Herein, the pillar width (w), the initial velocity (U_0), and density (ρ_l) of the droplet are chosen as the repeating variables, unless otherwise noted. Dimensional analysis shows that the droplet dynamics in this study is mainly dominated by the Weber number, $We_w = \rho_l U_0^2 w/\gamma$, Ohnesorge number, $Oh_w = \mu/\sqrt{\rho_l w\gamma}$, Bond number, $Bo_w = \frac{\rho_l g w^2}{\gamma}$, viscosity ratio, $\mu^* = \mu_l/\mu_v$, density ratio, $\rho^* = \rho_l/\rho_v$, droplet diameter, $D^* = D/w$, pillar height, $h^* = h/w$ and spacing $s^* = s/w$, the length, width, and height of the computational domain, $L^* = L/w$, and the dimensionless time $t^* = t/(\rho_l w^3/\gamma)^{0.5}$, where γ is the surface tension.

To facilitate the analysis, different types of energy of the droplet are considered, including the kinetic energy (E_{kin}), surface energy (E_{sur}), and dissipated energy (E_{dis}). The initial total energy of the droplet is defined as E_{tot}, including the initial surface energy and initial kinetic energy. Herein, we normalize all energies by E_{tot}. Specifically, the instantaneous kinetic energy of the droplet is defined as

$$E_{kin}^* = \int_V \rho U^2 dv/E_{tot}, \tag{14}$$

where V denotes the droplet volume. The surface energy of the droplet is expressed as[27]

$$E_{sur}^* = \gamma_{lv} A/E_{tot}, \tag{15}$$

where γ_{lv} denotes the surface tension of the droplet, and A is the surface area of the droplet. E_{dis}^* can be written as[27]

$$E_{dis}^* = \int_0^{\zeta}\int_V \frac{\mu_l}{2}(\nabla U + \nabla U^\dagger)^2 dvdt/E_{tot}, \tag{16}$$

where μ_l is the liquid viscosity. The dimensionless increment of surface energy is defined as

$$\Delta E_{sur}^* = (E_{sur,max} - E_{sur,0})/E_{tot}. \tag{17}$$

According to Hu et al.,[38] the impacting force in the vertical direction is defined as

$$F_z = \int_\Omega P n_z dA, \tag{18}$$

where P is the pressure, and Ω is the surface area of the droplet contacting with the SHS. The dimensionless impacting force can be written as

$$F^* = F_z/(\rho_l U_0^2 D_0^2), \tag{19}$$

where U_0 is the droplet initial velocity and D_0 is the droplet diameter.

C. Model validation

The numerical solver developed based on the above three-dimensional LBM-based pseudopotential model is validated by the following two cases. In the first one, a stationary droplet is placed at the center of computational domain with periodic boundary condition imposed on all boundaries, where the relaxation time $\tau = 1.0$ and the

domain length $L^* = 28$. In the equilibrium state, Fig. 2 shows that the pressure difference between the inside and outside of the droplet is inversely proportional to its radius. This accords with Laplace's law, where $\Delta P = 2\gamma/R_0$, with ΔP being the pressure difference and R_0 the droplet radius. Accordingly, $\gamma = 0.227$ in this validation case.

In the second case, a droplet normally impacting a flat surface is considered. The impingement dynamics is quantified by the normalized contact time $\tau_c = t_c/(R_0/U_0)We^{0.5}$, where t_c is the time period from contacting the surface to bouncing off, R_0 is the droplet radius, U_0 is the droplet initial velocity, and We is the Weber number defined based on R_0. Existing studies have demonstrated that there exists a linear relation between $\ln(\tau_c)$ and $\ln(1-\cos\theta)$ when the surface is hydrophobic and We ranges from 15 to 35, where θ is the contact angle,[22,39–44] as shown in Fig. 3. The simulation results (denoted by five-pointed star symbols in Fig. 3) yielded by the developed numerical solver for $We = 25$, and $\theta = 120°$, $140°$ and $160°$, can reproduce this relation, and $\ln(\tau_c)$ in these cases is close to that in the similar cases of other studies. These two validation cases demonstrate that the developed numerical solver can provide reliable simulation results for the droplet impact dynamics.

D. Grid independence verification

To ensure that the numerical results are independent of the mesh and time resolution, one case where the droplet impacts the SHS with the array of pillars described in Sec. II A is selected for the mesh resolution test, where the droplet diameter $D^* = 10.4$, the Weber number $We_w = 0.14$, the pillar height $h^* = 5$, the pillar spacing $s^* = 1$, and the contact angle is $\theta = 166.5°$ (see Fig. 4). Herein, the mesh spacing $\delta_x = w/5$ and the time step $\delta_t = t_{ca}/63$ (where $t_{ca} = (\rho_l w^3/\gamma)^{0.5}$ denotes the capillary time) in the coarse-resolution case, while $\delta_x = w/10$ and $\delta_t = t_{ca}/126\sqrt{2}$ in the fine-resolution case. Figures 4(a) and 4(b) illustrate that the droplet evolution and D_c/D_0 are independent of the mesh resolution. The time series of all the normalized energies in these two cases are nearly indistinguishable [see Fig. 4(c)]. Hence, $\delta_x = w/5$ and $\delta_t = t_{ca}/63$ are selected for the numerical simulation throughout this study.

Note that Eq. (11) denotes the interaction force between the fluid and surface, where G_s describes the strength of fluid–surface

interaction force and determines the surface wettability. Herein, G_s exhibits a linear relation with the contact angle (θ), as shown in Fig. 5. Specifically, $\theta = 7.13\,G_s + 195.26$ for G_s ranging from -22.0 to -4.0. In the mesh resolution test, G_s is selected as -4.0, which corresponds to $\theta = 166.5°$. This value is also adopted throughout this study.

E. Case summary

In this study, the computational domain is set as a cuboid with length $L^* = 28$. Both the density ratio ρ^* and dynamic viscosity ratio μ^* are selected as 36.5, corresponding to $T/T_{cr} = 0.8$ in Eq. (10). The gravitational effect is negligible with the Bond number Bo_w set below 0.008.[27] The intrinsic contact angle θ is chosen as $143.5°$ on the flat surface, corresponding to $G_s = -7.0$ in Eq. (11).

The droplet diameter D^* ranges from 8 to 14, and both the pillar spacing s^* and height h^* vary from 1 to 5. We_w is chosen from the range 0.14–3.57, while Oh_w is selected as 0.42. It should be noted that the effects of Oh on the impacting dynamics of droplet can be negligible when it is smaller than 1.0. Therefore, the findings in this study are applicable for some common droplets, such as water and ethanol droplets, whose Oh number is around 0.5.[27] The values of parameters are summarized in Table I. In the following, the influences of D^* and We_w are discussed first, followed by the effects of pillar spacing s^* and height h^*.

III. RESULTS AND DISCUSSION

A. Effects of D^* and We_w

For a more cohesive discussion, we will simultaneously discuss Fig. 6 for the morphology of the droplet and Fig. 7 for time series of its diameter change, energy, and impacting force. Figure 6 shows the droplet shape evolution in the two representative cases at Weber number $We_w = 0.14$ and 3.57 when the droplet of diameter $D^* = 10.4$ impacts the SHS with pillar height $h^* = 5$ and spacing $s^* = 1$. Herein, the instant when the droplet starts to contact the pillars is defined as $t^* = 0$.

In the case when $We_w = 0.14$, the droplet gradually deforms and spreads on top of the pillars after $t^* = 0$, as shown in Figs. 6(a1) and 6(a2). At $t^* = 3.81$, the contacting factor (defined as the ratio of the diameter of the droplet's cross section intersecting the top surfaces of
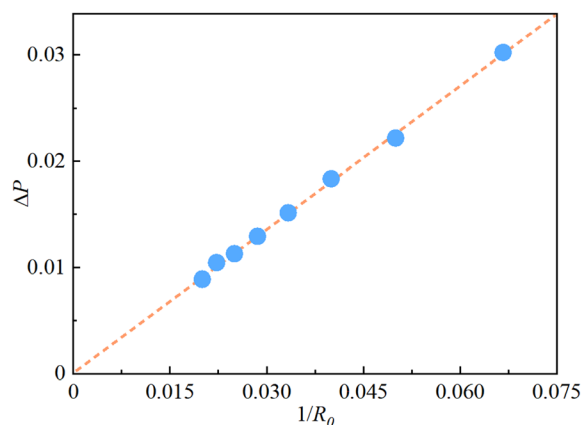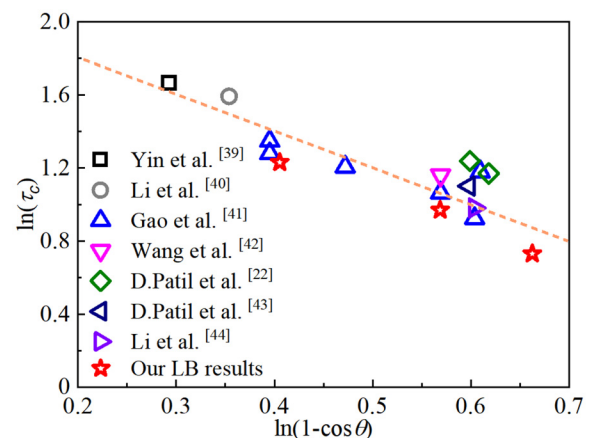

FIG. 2. Variation of ΔP with $1/R_0$.

FIG. 3. Variation of $\ln(\tau_c)$ with $\ln(1-\cos\theta)$.[22,39–44]

FIG. 4. (a) Droplet shape evolution (red: $\delta_x = w/5$ and $\delta_t = 1/63t_{ca}$; black: $\delta_x = 2w/5$ and $\delta_t = 2/63t_{ca}$), (b) variation of D_c/D_0 vs time, and (c) time histories of E_{sur}^* (square), E_{kin}^* (circle), E_{dis}^* (triangle), and E_{tot}^* (inverted triangle) when $\delta_x = w/5$ and $\delta_t = 1/63t_{ca}$ (dark gray color) and $\delta_x = 2w/5$ and $\delta_t = 2/63t_{ca}$ (pale blue) for $D^* = 10.4$, $We_w = 0.14$, $h^* = 5$, $s^* = 1$, and $\theta = 166.5°$.
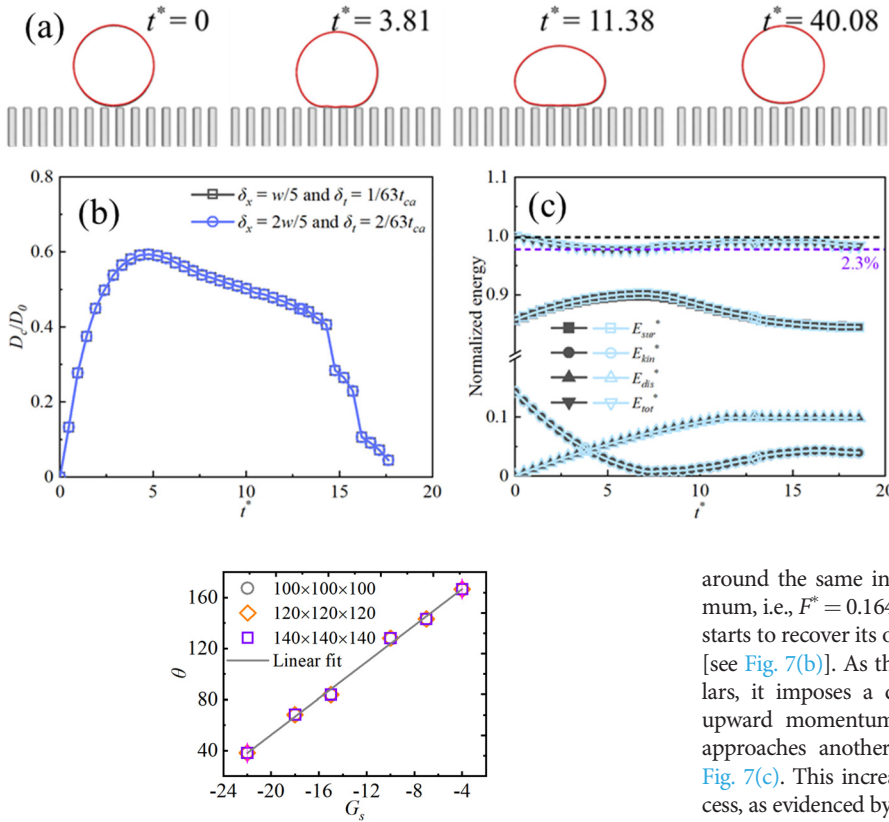

FIG. 5. Variation of contact angle of droplet (θ) on the smooth surface vs G_s.

pillars to the droplet initial diameter) approaches its maximum, i.e., $D_c/D_0 = 0.593$, as shown in Fig. 7(a). During this process, the impacting force also approaches its maximum, i.e., $F^* = 0.801$ [see Fig. 7(c)], and the kinetic energy (E_{kin}^*) is gradually converted to the surface energy (E_{sur}^*), accompanied by a small amount of energy dissipation quantified by E_{dis}^*, as shown in Fig. 7(b).

As time advances, the droplet remains stuck to the pillars with negligible overall movement, and D_c/D_0 remains large and gradually decreases at a much smaller rate, while E_{kin}^* is close to zero, as shown in Figs. 7(a) and 7(b). By contrast, the droplet keeps deforming and approaches the largest overall deformation at $t^* = 8.58$, at which instant E_{sur}^* approaches its maximum, as shown in Fig. 7(b). At

TABLE I. Definition and selected values of key non-dimensional parameters in this study.

Dimensionless parameter	Definition	Value
Droplet diameter	$D^* = D/w$	8–14
Pillar spacing	$s^* = s/w$	1–5
Pillar height	$h^* = h/w$	1–5
Weber number	$We_w = \rho_l U_0^2 w / \gamma$	0.14–3.57
Radius-based Weber number	$We = D^* We_w / 2$	1.43–35.68
Ohnesorge number	$Oh_w = \mu / \sqrt{\rho_l w \gamma}$	0.42

around the same instant, the impacting force reaches its local minimum, i.e., $F^* = 0.164$ [see Fig. 7(c)]. Immediately after that, the droplet starts to recover its original shape, as evidenced by the decreasing E_{sur}^* [see Fig. 7(b)]. As the droplet still contacts the top surfaces of the pillars, it imposes a downward force on the pillars and obtains the upward momentum for bouncing off. As such, the impact force approaches another maximum at around $t^* = 12.39$, as shown in Fig. 7(c). This increase in impact force expedites the bounce-off process, as evidenced by an increase in the decreasing rate of D_c/D_0 shown in Fig. 7(a). During this period, surface energy is gradually converted to kinetic energy, as shown in Fig. 7(b). At around $t^* = 17.63$, D_c/D_0 approaches zero, and the droplet completely leaves the SHS, as shown in Figs. 6(a4) and 7(a).

When $We_w = 3.57$, the droplet impacts and spreads on the top of the pillar arrays from $t^* = 0$ to 3.79, as shown in Figs. 6(b1)–6(b3). During this period, D_c/D_0 and F^* gradually approach their maxima, i.e., 1.40 and 0.803, respectively, as shown in Figs. 7(a) and 7(c), and the kinetic energy is converted to the surface energy, along with energy dissipation, as shown in Fig. 7(b). At the same time, the lower part of the droplet penetrates the pillar arrays and gets into the gaps, as shown in Figs. 6(b2) and 6(b3). Although the variations of D_c/D_0 with t^* are similar for $We_w = 0.14$ and 3.57 during this period, the droplet impingement in these two cases is different. Compared to the case of $We_w = 0.14$ where the droplet stays above the pillars, evident penetrations are exhibited in the case of $We_w = 3.57$. This mainly stems from the fact that the kinetic energy of the droplet is larger when $We_w = 3.57$, resulting in a more intense impact. For the same reason together with the induced penetration phenomenon, a much faster conversion from the kinetic to surface energy is exhibited and faster energy dissipation occurs, as shown in Fig. 7(b). Furthermore, unlike in the case when $We_w = 0.14$, the instant at which E_{kin}^* approaches its minimum is ahead of that at which D_c/D_0 approaches its maximum in the case when $We_w = 3.57$. This is associated with the fact that the droplet motion is mainly stopped by the pillars before complete spreading of the droplet. As such, the maximum F^* approaches its maximum earlier when $We_w = 3.57$, as shown in Fig. 7(b).
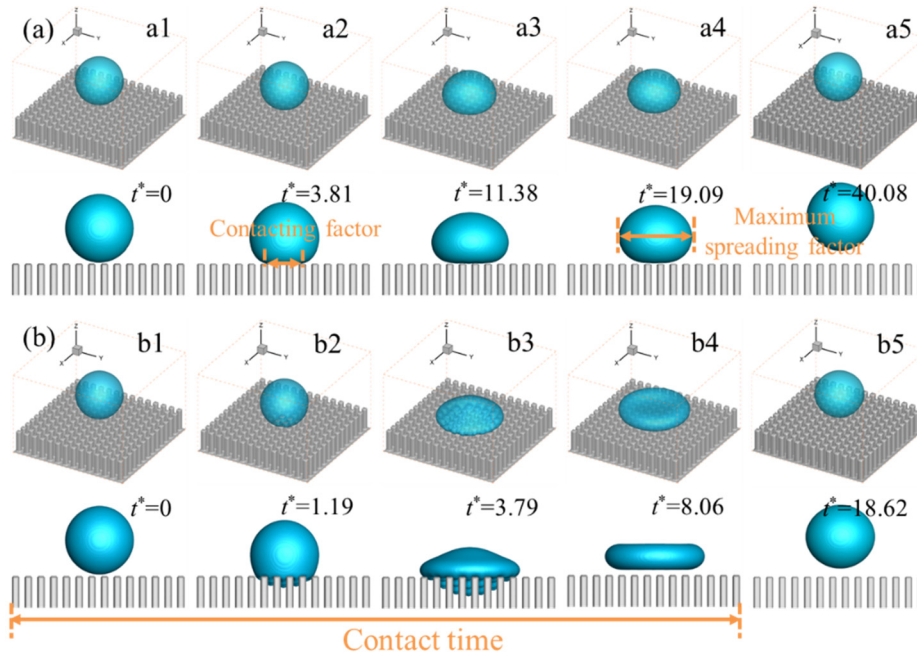
FIG. 6. Droplet shape evolution when impacting on an SHS with pillar arrays: (a) $We_w = 0.14$ and (b) $We_w = 3.57$.

After spreading to the maximum diameter, the part of the droplet in the pillar gaps starts to retract fast while the top part of the droplet continues moving downward at a small speed. The fast retraction of the bottom part of the droplet causes the surface energy to decrease and converts it into kinetic energy rapidly (see Fig. 7b). At around $t^* = 5.5$, E_{kin}^* approaches its local maximum, i.e., $E_{kin}^* = 0.209$, while E_{sur}^* reaches its local minimum, i.e., $E_{sur}^* = 0.282$. Such a fast retraction of the droplet among pillar gaps causes rapid separation of the droplet bottom from pillar tops. As a result, at $t^* = 7.38$ the droplet completely leaves the pillars and bounces off the surface with a pancake shape roughly before it begins to recover the spherical shape, as shown in Fig. 6(b4). During this period, D_c/D_0 and F^* monotonically decrease to 0, as shown in Figs. 7(a) and 7(c).

Compared to the case when $We_w = 0.14$, the conversion from surface to kinetic energy is faster in the case when $We_w = 3.57$. This stems from the fast droplet retraction among pillar gaps for $We_w = 3.57$ while no penetration is exhibited for the case when $We_w = 0.14$. Furthermore, unlike the case when $We_w = 0.14$ where the droplet recovers to the original shape when it sits on the top of pillars yielding a second peak of F^*, the droplet with $We_w = 3.57$ has been detached from the pillars before major recovery to the original shape, as shown in Figs. 6(a3) and 6(b4). As such, only one peak for F^* is presented in the case when $We_w = 3.57$. Even though complete distinct droplet impact dynamics, the global maximum F^* is independent of We_w, as shown in 7(c).

The above analysis clearly shows the dependence of droplet impingement dynamics and contact time (t_c^*) on We_w. When We_w is small, the droplet exhibits slow bouncing, while it undergoes fast bouncing (corresponding to small t_c^*), usually named as "pancake bouncing,"[19] when We_w is sufficiently large. Moqaddam *et al.*[27] figured
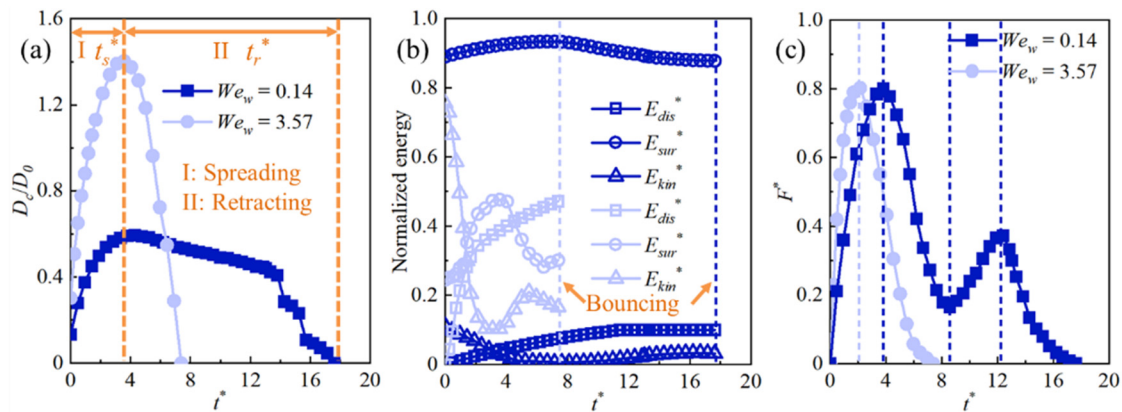

FIG. 7. Time histories of (a) D_c/D_0, (b) E_{dis}^*, E_{sur}^*, E_{kin}^*, and (c) F^* when $We_w = 0.14$ (navy blue color) and 3.57 (pale blue color).

out that the reduction of t_c^* is positively associated with increase in the surface energy. This can be further corroborated by the above two cases, where the maximum increment of surface energy $\Delta E_{sur}^* = 0.044$ and 0.232 for $We_w = 0.14$ and 3.57, respectively, and $t_c^* = 17.63$ and 7.38, respectively.

When $h^* = 5$ and $s^* = 1$, the dynamic behaviors of the droplet in the cases with other values of We_w and D^* are similar to either the case with $We_w = 0.14$ or 3.57 and $D^* = 10.4$. Therefore, the detailed dynamic behaviors and impingement process are not repeated for each We_w and D^* for the sake of space, while only the key quantities representing the impact dynamics are given and discussed for these cases. In the following, we will show the trend of varying D^* and We_w for a comprehensive evaluation of the effect of these parameters.

Figure 8 shows the time histories of D_c/D_0 at different D^* and We_w. When $We_w = 0.14$, D_c/D_0 increases rapidly to the maximum with time and then decreases to 0 slowly for all D^*, as shown in Fig. 8(a), meaning that the droplet spreading time (t_s^*) is shorter than its retracting time (t_r^*), where t_s^* is defined as the time from starting to contact the pillars to the maximum spreading, and the retracting time is defined as $t_r^* = t_c^* - t_s^*$. Additionally, the maximum D_c/D_0 and t_s^* increase with D^*, while t_c^* approaches its maximum at an intermediate D^*, i.e., $D^* = 11.6$.

When We_w increases to 0.57, the initial kinetic energy of the droplet augments, resulting in a larger D_c/D_0, as shown in Fig. 8(b). This can be further evidenced by the scaling relation $D_{max}/D_0 \sim We_w^{03}$ revealed in Fig. 8(f), where D_{max}/D_0 is the maximum spreading factor that is defined as the maximum circumferential diameter of the droplet observed from top view to the droplet initial diameter [see Fig. 6(a4)]. Since t_s^* remains roughly unchanged, the increasing rate of D_c/D_0 becomes larger. On the other hand, the variation trend of D_c/D_0

and influences of D^* roughly remain the same when We_w increases from 0.14 to 0.57, as shown in Fig. 8(b).

Compared to when $We_w \leq 0.57$, the increasing rate of D_c/D_0 is larger than that when $We_w \geq 1.28$ but the droplet spreading time remains roughly unchanged, as shown in Fig. 8. The retraction rate of the droplet is faster when $We_w \geq 1.28$, arising from the change in bouncing-off patterns of the droplet, as mentioned above. Therefore, t_c^* is smaller when $We_w \geq 1.28$.

The variation of t_c^* with We_w and D^* is summarized in Fig. 9. When $We_w \geq 1.28$, t_c^* increases with D^* generally in a linear manner, while it approaches its maximum at $D^* = 11.6$ for $We_w \leq 0.57$. Furthermore, t_c^* in the cases when $We_w \geq 1.28$ is much smaller than that in the case when $We_w \leq 0.57$ for each D^*. However, t_c^* does not decrease monotonically with We_w when $We_w \geq 1.28$, and it approaches its minimum when $We_w = 2.28$. This could be due to the fact that when We_w is over a critical value between $We_w = 1.28$ and 3.57, the portion of the droplet penetrating the pillar gaps increases, which requires more time for retraction during bouncing off. Therefore, to achieve maximum reduction of the contact time, one needs find a proper We_w.

Figure 10 shows E_{dis}^*, ΔE_{sur}^*, and the normalized kinetic energy when the droplet bounces off the surface ($E_{kin,\,b}^*$) for different We_w and D^*. It is seen that E_{dis}^* increases with We_w and D^*, as shown in Fig. 10(a). This arises from the fact that the droplet with a larger We_w or D^* (corresponding to a larger initial velocity or size and the resulting larger $E_{kin,\,b}^*$ at $t^*=0$) undergoes a more violent collision with the SHS and could penetrate more into the gaps among the pillars. As such, more energy can be dissipated before it bounces off the surface. For the same reason, ΔE_{sur}^* generally increases with We_w and D^*. Furthermore, $E_{kin,\,b}^*$ is almost independent of D^*, while it approaches its local maximum when $We_w = 2.28$ for each D^*.
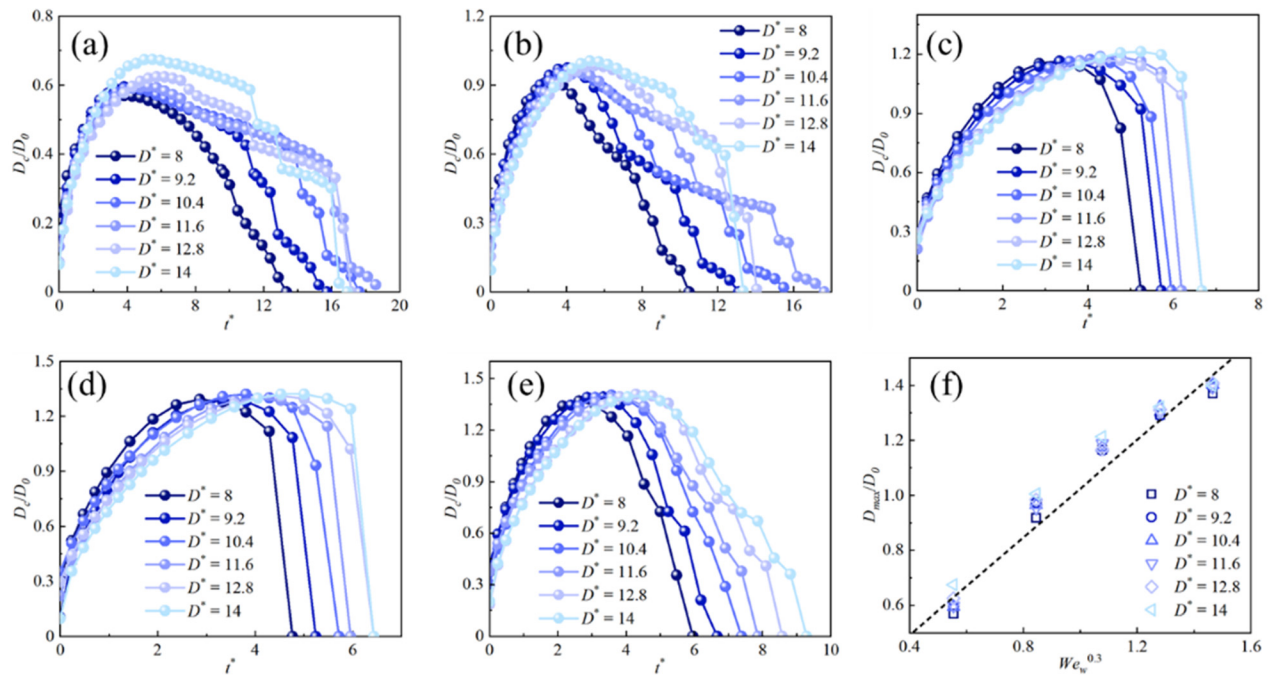

FIG. 8. Time histories of D_c/D_0 for $D^* = 8$–14 when (a) $We_w = 0.14$, (b) $We_w = 0.57$, (c) $We_w = 1.28$, (d) $We_w = 2.28$, and (e) $We_w = 3.57$. Variation of D_{max}/D_0 with We_w^{03}.
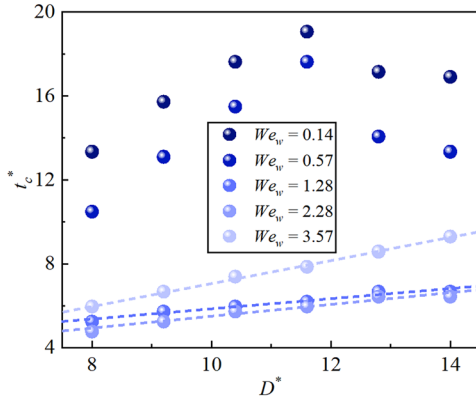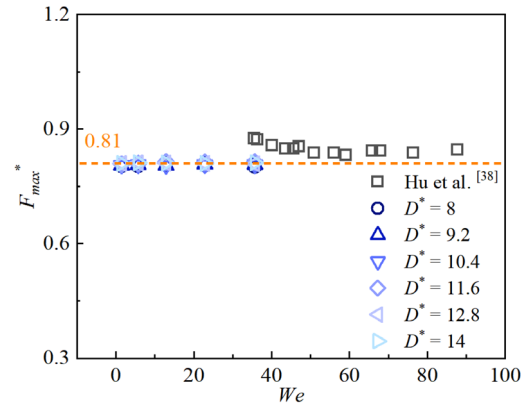
FIG. 9. Variation of t_c^* with D^* for different We_w.

**FIG. 11.** Variation of F_{max}^* with We.

Figure 7(c) reveals that the maximum impacting force (F_{max}^*) is independent of We_w in the cases with $We_w = 0.14$ and 3.57 when $D^* = 10.4$. Such an independent relation remains for all We_w. F_{max}^* is also independent of D^*, as shown in Fig. 11, where $F_{max}^* \approx 0.81$. This finding agrees well with those given in Hu et al.,[38] where $F_{max}^* \approx 0.85$ at higher We. Herein, $We = D^* We_w/2$ is adopted for comparison with the finding in Hu et al.[38]

B. Effects of s^* and h^*

Next, we study the change of the geometry of the SHS on the droplet impingement dynamics. Figure 12 shows the shape evolutions of the droplet of diameter $D^* = 10.4$ in five representative cases with pillar height h^* ranging from 0 to 5 and pillar spacing s^* ranging from 0 to 5 ($h^* = 0$ or $s^* = 0$ corresponds to the flat surface), when the Weber number $We_w = 2.28$. For h^* ranging from 0 to 5, the droplet shape evolutions are similar, as shown in Figs. 12(a), 12(d), and 12(e). The variation trends of the kinetic, surface, and dissipated energies with time and their maximum or minimum values are roughly the same in all these cases, as shown in Figs. 13(a), 13(d), and 13(e). However, the impingement and bouncing-off processes of the droplet differ in these cases.

In the cases when $h^* = 1$ and 5, the droplet gets into the gaps among pillars during impingement, like in the case when $We_w = 3.57$ and $D^* = 10.4$ discussed in Sec. III A. Such a penetration speeds up the conversion of kinetic to surface energy during droplet rebounding. This enables the droplet to leave the surface just when it exhibits a pancake shape, as shown in Figs. 12(a5) and 12(d6). By contrast, when $h^* = 0$, the surface is flat, and the droplet remains stuck to the surface for a longer time. Even though the droplet also exhibits a pancake shape during rebounding, as shown in Fig. 12(e4), at such an instant the bottom of the droplet is still in touch with the surface and does not leave the surface like it does when $h^* = 1$ and 5. This means that energy conversion among the pillars can accelerate the energy conversion rate and hence reduces the contact time (t_c^*). This accounts for the contact time reduction in the cases when $h^* = 1$ and 5 compared to the case when $h^* = 0$. The smallest t_c^* can be achieved at $h^* = 1$, indicating that the critical h^* for the fastest bouncing is around 1.

It is interesting to note that in these cases, the maximum surface energy is generally the same, indicating that the droplet deforms to similar extents. Unlike in the cases when $h^* = 1$ and 5 where the increment in surface energy stems from the droplet's penetration into the pillars and deformation of the droplet above the pillars, no pillars are involved in the flat-surface case with $h^* = 0$. As such, the increment in
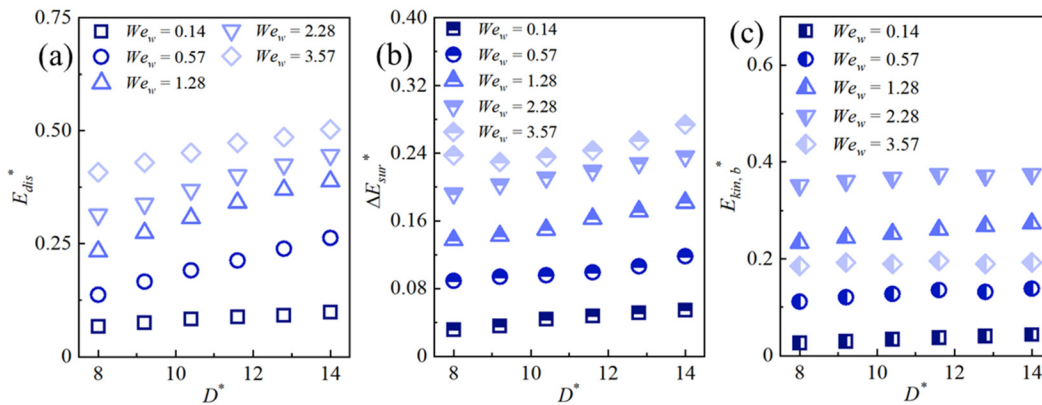
FIG. 10. Variation of (a) E_{dis}^*, (b) ΔE_{sur}^*, and (c) $E_{kin, b}^*$ with D^* for different We_w.
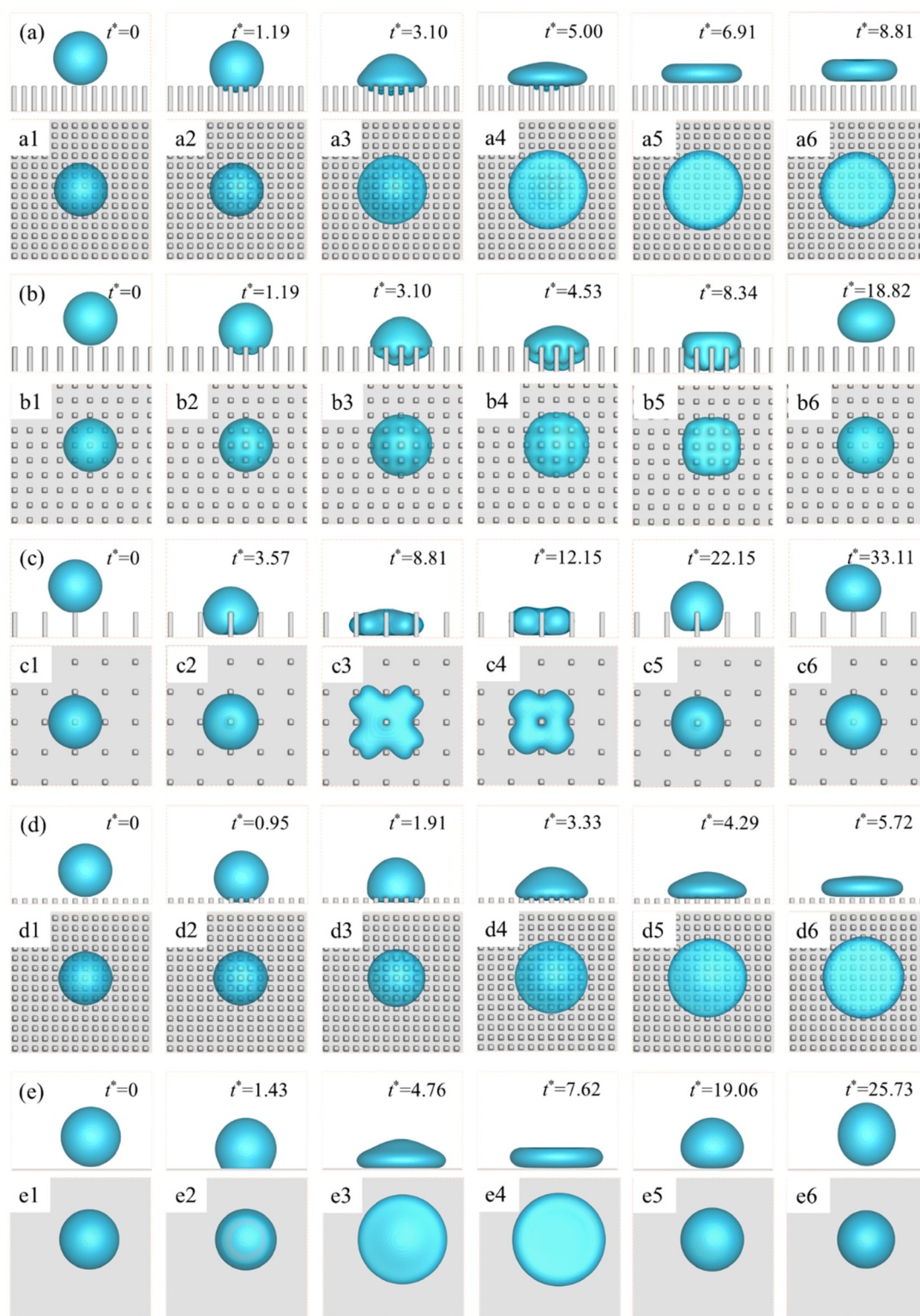
08 December 2025 09:23:46

FIG. 12. Droplet shape evolution when $D^* = 10.4$ and $We_w = 2.28$: (a) $s^* = 1$, $h^* = 5$; (b) $s^* = 2$, $h^* = 5$; (c) $s^* = 5$, $h^* = 5$; (d) $s^* = 1$, $h^* = 1$, and (e) $s^* = 0$ or $h^* = 0$ (corresponding to a flat surface).
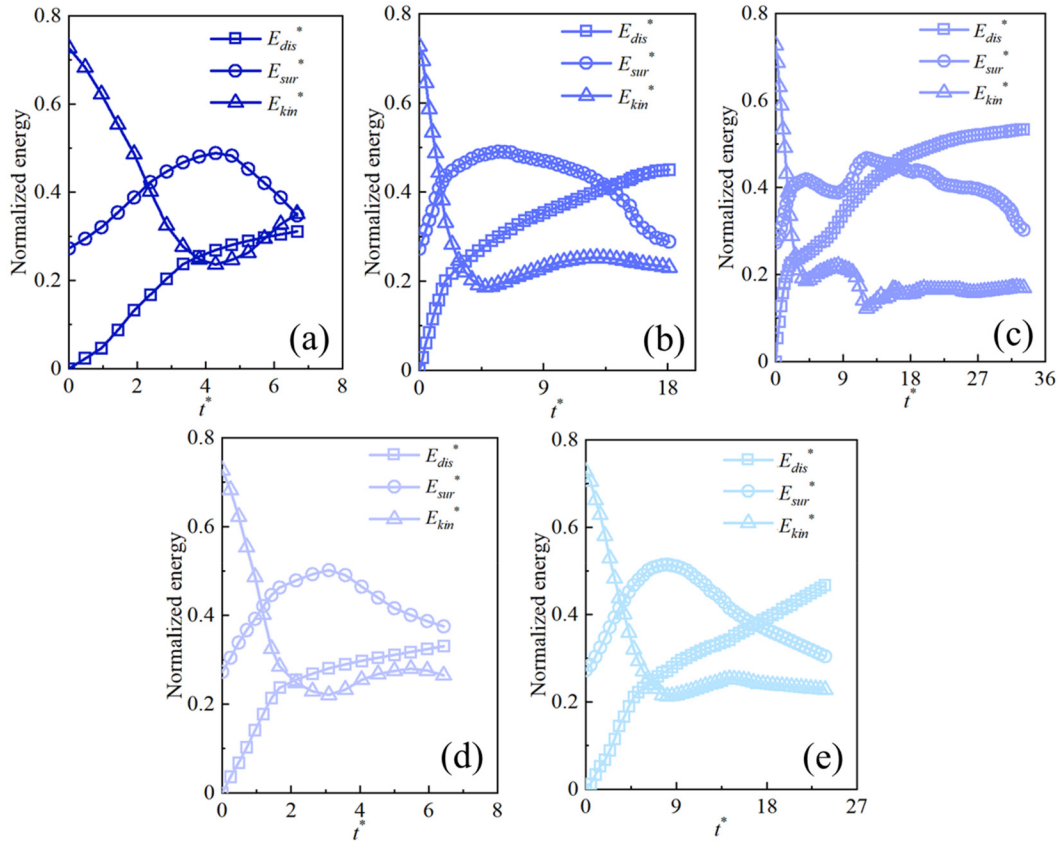
FIG. 13. Time histories of E_{dis}^*, E_{sur}^*, and $E_{kin,\,b}^*$ for (a) $s^* = 1$ and $h^* = 5$, (b) $s^* = 2$ and $h^* = 5$, (c) $s^* = 5$ and $h^* = 5$, (d) $s^* = 1$ and $h^* = 1$, and (e) $s^* = 0$ or $h^* = 0$ (corresponding to a flat surface).

surface energy can only be caused by droplet deformation above the surface. Under this condition, droplet deformation above the surface is larger when $h^* = 0$, associated with the greater maximum contacting factor (D_c/D_0), as shown in Fig. 14(a).

Compared to those of h^*, the influences of s^* on droplet impacting dynamics are more evident, which can be seen by comparing the four representative cases with $s^* = 0$, 1, 2, and 5 when $h^* = 5$, among which the cases when $s^* = 0$ and 1 have been discussed above. Note that the case with $s^* = 0$ corresponds to the case without pillars and hence is the same as that with $h^* = 0$.

Unlike in the case when $s^* = 1$ where only a small portion of the droplet can penetrate the pillar arrays, the penetration is much more pronounced in the case when $s^* = 2$, if comparing the first and second rows of Fig. 12. This stems from the smaller resistance imposed on the droplet by the pillars for larger s^*. Such a deep penetration causes fast energy dissipation right after the droplet just impacts the pillars. This is evidenced by the fact that the normalized dissipated energy (E_{dis}^*) increases from 0 to 0.2 from $t^* = 0$ to 1.91 when $s^* = 2$, while the period for the same increment of E_{dis}^* is from $t^* = 0$ to 2.86 when $s^* = 1$, as shown in Fig. 13(b). For the same reason, the spreading process of the droplet is also delayed, as shown in Fig. 14(a), where the instant at which D_c/D_0 approaches its maximum is around $t^* = 5.72$. In addition, the spreading of the droplet is constrained by the nearby

pillars. Under this condition, the maximum D_c/D_0 is smaller in the case when $s^* = 2$. The deep penetration also prolongs the retraction process of the droplet and retards the related energy conversion process. This can be seen from the slower variation of E_{sur}^* and normalized kinetic energy (E_{kin}^*) after the maximum E_{sur}^* is approached in the case when $s^* = 2$ than in the case when $s^* = 1$, as shown in
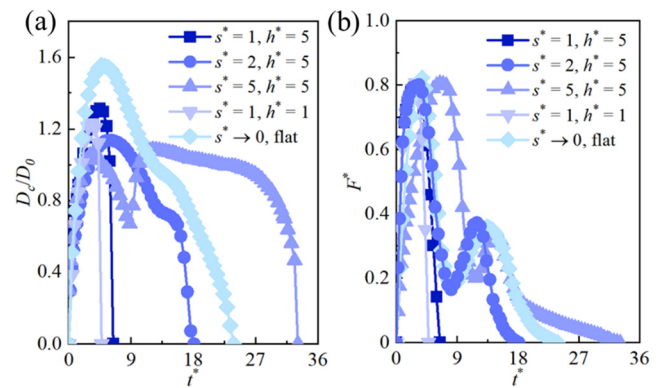

FIG. 14. Time histories of (a) D_c/D_0 and (b) F^* for different s^* and h^*.

Figs. 13(a) and 13(b). Eventually, the droplet bounces off the surface in an ellipsoidal shape [see Fig. 12(b6)].

When s^* increases to 5, the gaps among pillars become larger and the resistance force of the pillars on the downward-moving droplet is smaller. As such, during impingement, the droplet directly encapsulates the pillar below it, impacts the side surfaces of the eight neighboring pillars and the base surface of the pillars, and presents a cloverleaf shape, as shown in Figs. 12(c1)–12(c3). Owing to the sparser arrangement of pillars, less constraint is imposed to stop subsequent spreading of the droplet, compared with that in the case when $s^* = 2$. As such, the spreading is more appreciable when $s^* = 5$, as demonstrated in Figs. 12(b4) and 12(c3). For the same reason, the overall energy conversion process when $s^* = 5$ is slower than when $s^* = 2$. For instance, the maximum E_{sur}^* and minimum E_{kin}^* can be achieved at around $t^* = 12.15$ when $s^* = 5$, while those can be obtained earlier at around $t^* = 5.72$ when $s^* = 2$, as shown in Figs. 13(b) and 13(c). Furthermore, when $s^* = 5$ the interaction between the droplet and the base surface of the pillars is also intensively involved from $t^* = 3.57$ to $t^* = 20.25$, just like in the case without pillars shown in Fig. 12(e), while this does not occur when $s^* = 2$ despite deep penetration. This causes a slower energy conversion process during retraction of the droplet when $s^* = 5$.

Despite different droplet impact dynamics exhibited in the above representative cases, the maximum impacting force (F_{max}^*) remains nearly the same, i.e., $F_{max}^* \approx 0.808$, as shown in Fig. 14(b). This value also remains roughly unchanged for other h^* and s^*, as shown in Fig. 15. Furthermore, $F_{max}^* \approx 0.808$ for other We_w and D^*, as given in the previous section. This means that F_{max}^* is independent of We_w, D^*, h^*, and s^*. Additionally, another local maximum of F^* can be exhibited if the droplet remains in contact with the pillars during retraction, such as that in the associated cases discussed in Figs. 7(c) and 14(b), and its value remains approximately 0.35, and is roughly independent of the above parameters. The value is also close to the one given by Li et al.,[37] which is 0.45. This means that the finding in Hu et al.[37] where only a flat SHS is considered is also applicable to more general scenarios where pillars of different arrangements are integrated with the SHS.

Figure 16 summarizes the maximum spreading factor (D_{max}/D_0) and t_c^* in the cases with h^* ranging from 0 to 5 and s^* ranging from 0 to 5 when D^* varies from 8 to 14. When $h^* = 5$, D_{max}/D_0 mainly changes with s^* and is generally independent of D^*, as shown in Fig. 16(a). D_{max}/D_0 approaches its minimum at $s^* = 2$ due to the evident constraint of pillars on the lateral spreading of the droplet, as revealed above. Additionally, for each D^*, t_c^* is the smallest at $s^* = 1$, since the droplet can bounce off the pillars with pancake shape, as shown in Figs. 12(a) and 16(b). For each s^*, t_c^* is roughly proportional to D^* (indicated by the consistent collapse of t_c^*/D^* at each s^*), meaning that larger droplet undergoes slower bouncing. In the cases when $s^* = 1$ and $h^* \geq 1$ where pancake bouncing is present, D_{max}/D_0 is roughly independent of D^*, and it remains smaller than 1.32, as shown in Figs. 12(a), 12(d), and 16(c). D_{max}/D_0 approaches its minimum at $h^* = 1$ and saturates when $h^* \geq 3$, and so does t_c^*, as shown in Fig. 16(d). The above relations of t_c^* with h^* and s^* imply that there exist optimal h^* and s^* between 0 and 3 for the smallest t_c^*.

The effect of s^* on E_{dis}^*, the maximum increment of normalized surface energy (ΔE_{sur}^*), and the normalized kinetic energy when bouncing off the surface ($E_{kin, b}^*$) for D^* ranging from 8 to 14 are
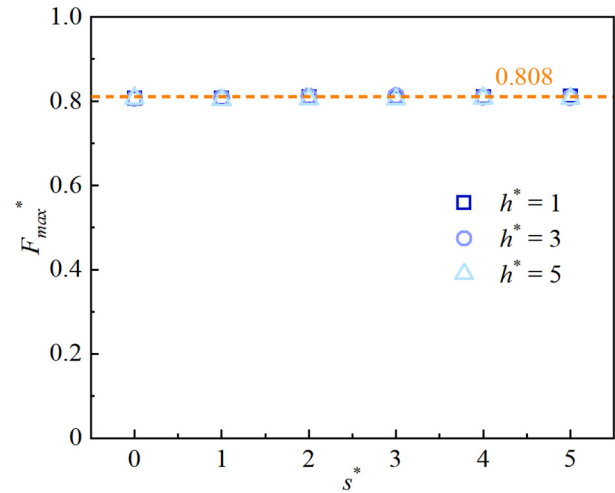

FIG. 15. Variation of F_{max}^* with s^* for $h^* = 1$, 3, and 5.

revealed in Fig. 17. Specifically, E_{dis}^* and ΔE_{sur}^* approach local minimum at $s^* = 1$ and 2, respectively, while they generally increase with D^*. Additionally, $E_{kin, b}^*$ is less dependent on D^* and approaches its maximum at $s^* = 1$. The influence of h^* can be seen in Fig. 18. In particular, for each D^*, E_{dis}^* and ΔE_{sur}^* generally decrease when h^* increases from 0 to 1, while their changes are less evident when h^* further increases to 5. $E_{kin, b}^*$ increases with h^* first and then levels off at $h^* \geq 3$.

C. Effects of the increment of surface energy (ΔE_{sur}^*) and energy conversion rate (ΔE_{sur}^*) on t_c^*

Moqaddam et al.[27] revealed that the reduction of contact time (t_c^*) is positively correlated with increase in the surface energy of the droplet. This can be confirmed by the cases discussed in Sec. III A of this study, where the Weber number (We_w) varies from 0.14 to 3.57 and the droplet diameter (D^*) is in the range of 8–14. Particularly, Fig. 19(a) shows t_c^* vs the increment of surface energy (ΔE_{sur}^*). It is seen that when ΔE_{sur}^* is larger than a critical value, i.e., $\Delta E_{sur,c}^* = 0.12$, t_c^* is generally smaller than that when $\Delta E_{sur}^* < \Delta E_{sur,c}^*$.

By contrast, such a relation is not applicable for the cases discussed in Sec. III B where both the arrangement of pillars changes and the pillar height (h^*) and spacing (s^*) vary from 0 to 5. This is demonstrated by Figs. 19(b) and 19(c). For instance, in the case $s^* = 1$, the droplet can bounce off the pillars with pancake shape and yield the smallest t_c^*. However, ΔE_{sur}^* is generally smaller than that in the case when $s^* = 0$ where pancake bouncing is not present, as shown in Fig. 19(b). Such discrepancies could be due to the fact that the variations of h^* and s^* are not considered in Moqaddam et al.,[27] and the finding in that study is not sufficiently general to be applied in other types of cases.

The analysis in the previous sections shows that when the conservation rate of the surface energy to kinetic energy is faster, rapid rebounding can be achieved. This indicates that the rate of energy conversion from kinetic to surface energy could be a good indicator for determining the impacting and rebounding speed of the droplet and thus the contact time. Herein, such an energy conversion rate is
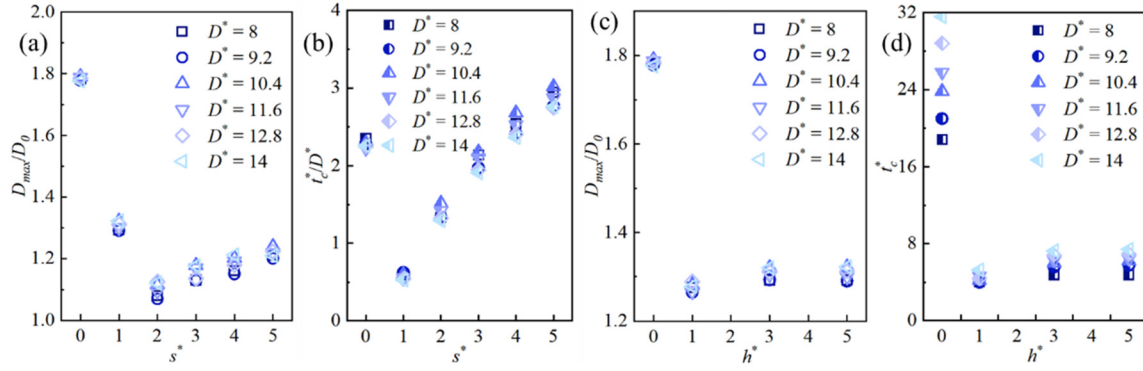
FIG. 16. Variation of (a) D_{max}/D_0 and (b) t_c^*/D^* with s^* when $h^* = 5$, and variation of (c) D_{max}/D_0 and (d) t_c^* with h^* when $s^* = 1$.
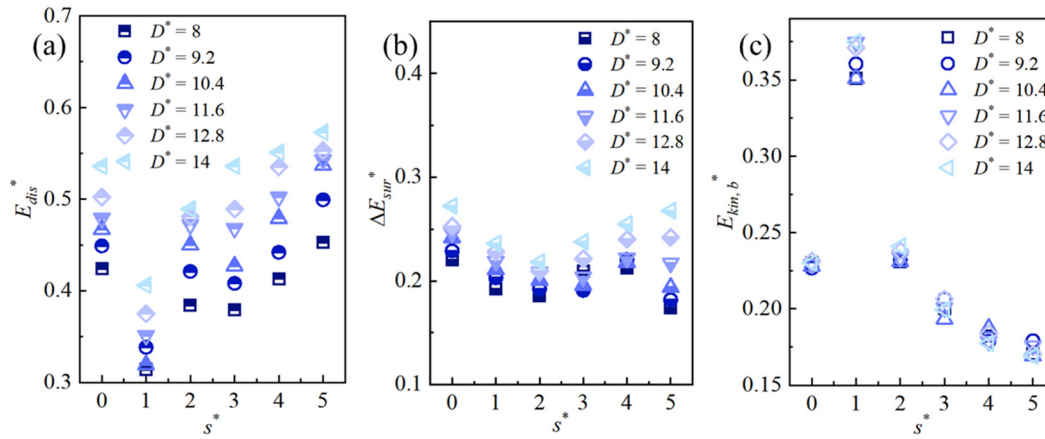

FIG. 17. Variation of (a) E_{dis}^*, (b) ΔE_{sur}^*, and (c) $E_{kin,\,b}^*$ with s^* for D^* ranging from 8 to 14 when $We_w = 2.28$ and $h^* = 5$.
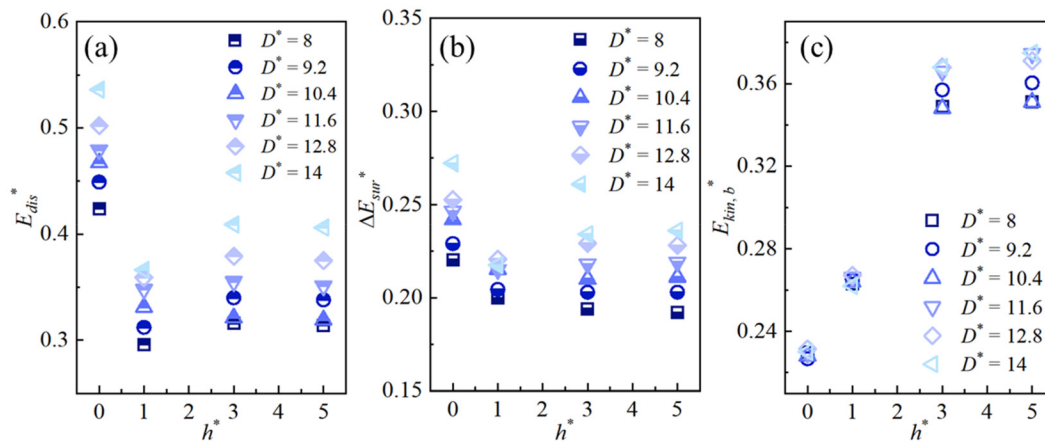

FIG. 18. Variation of (a) E_{dis}^*, (b) ΔE_{sur}^*, and (c) $E_{kin,\,b}^*$ with h^* for D^* ranging from 8 to 14 when $We_w = 2.28$ and $s^* = 1$.
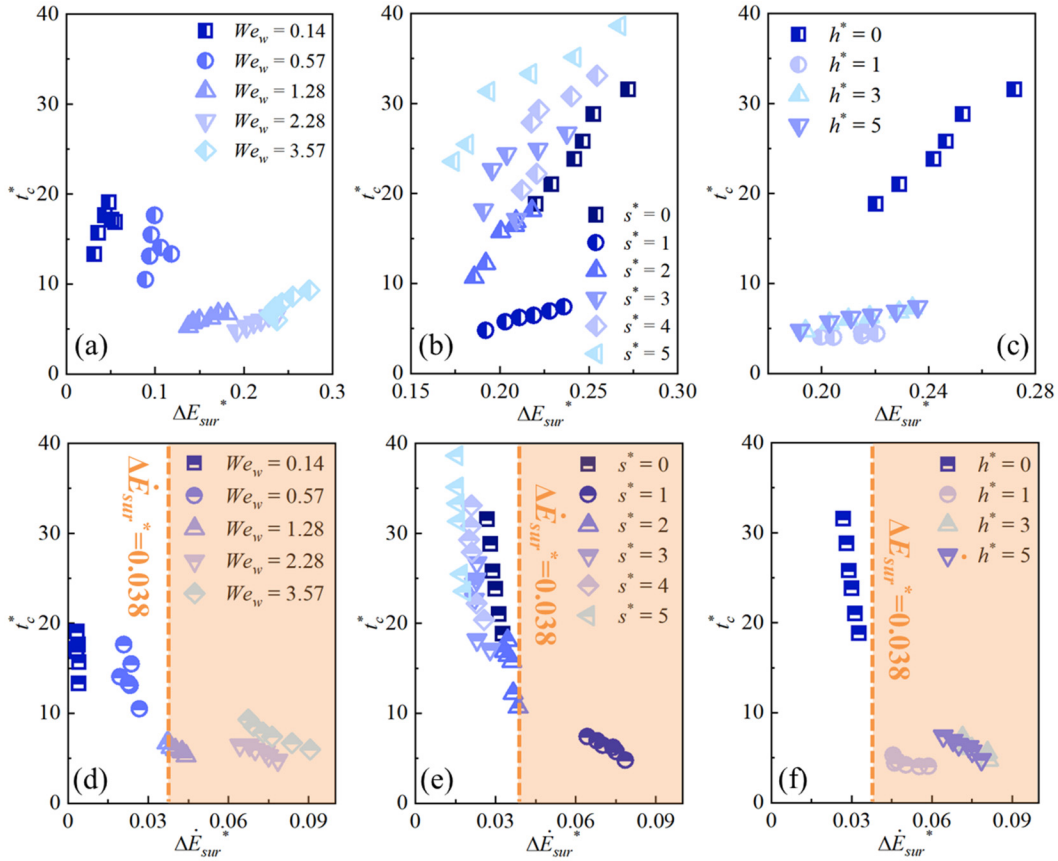
FIG. 19. Variation of t_c^* with ΔE_{sur}^* for different (a) We_w, (b) s^*, and (c) h^*. Variation of t_c^* with $\Delta \dot{E}_{sur}^*$ for different (d) We_w, (e) s^*, and (f) h^*.

defined as $\Delta \dot{E}_{sur}^* = \Delta E_{sur}^*/\Delta t_E^*$, where Δt_E^* denotes the period over which the surface energy approaches its maximum from $t^* = 0$. $\Delta \dot{E}_{sur}^*$ vs t_c^* is plotted in Figs. 19(d)–19(f). In each subfigure, the cases can be separated into two distinct regimes by a vertical line at $\Delta \dot{E}_{sur}^*$ with a value of approximately 0.038. Cases with small t_c^* are predominantly clustered on the right of this line. This indicates that $\Delta \dot{E}_{sur}^*$ could be a more general metric for determining whether small t_c^* is attainable.

IV. CONCLUSIONS

This study furthers our understanding of the droplet impact dynamics when it impinges on a superhydrophobic surface (SHS) patterned with sparse/dense and tall/short square pillar arrays and extends the findings of previous studies, by exploring the impact dynamics of a droplet when its diameter D^* ranges from 8 to 14, the Weber number We_w ranges from 0.14 to 3.57, the pillar spacings s^* range from 1 to 5, and the pillar heights h^* range from 1 to 5. The major findings are summarized as follows:

(i)   The droplet's bouncing pattern turns from normal to pancake with We_w increasing from 0.14 to 3.57, rendering a significant reduction in contact time (t_c^*). The type of bouncing pattern is generally independent of D^*, and t_c^* linearly increases with D^* when pancake bouncing is exhibited.

(ii)   The bouncing pattern varies with the specific design of the SHS, including h^* and s^*. Pancake bouncing can be achieved at a sufficiently large h^*, i.e., $h^* \geq 1$, and an intermediate s^*, i.e., $s^* \approx 1$. In other cases, the droplet is either stuck to the SHS (such as when $h^*=1$) or confined among the pillars (such as when $s^*=5$) and undergoes slow rebounding. Hence, to achieve a small t_c^*, a moderate s^* and a large h^* are desired.

(iii) The impacting force usually approaches a large peak during the impacting process and a small peak during the rebounding process for normal bouncing, while only a large peak is present for pancake bouncing. In all cases, the values of these two peaks are independent of D^*, We_w, s^*, or h^*. The value of the large peak is around 0.81, and that of the small one is close to 0.35. These are generally in accord with those presented in Hu et al.,[37] where only the droplet impinging a flat surface is considered.

(iv)   Small t_c^* can be achieved when the increment of the normalized surface energy ΔE_{sur}^* is sufficiently large for $s^* = 1$ and $h^* = 5$. This agrees well with the findings by Moqaddam et al.[27] However, this relation is not applicable to more complex scenarios where sparse or short pillars are considered. Our analysis reveals that t_c^* is not primarily determined by

ΔE_{sur}^* itself but rather by its rate of change, i.e., $\Delta \dot{E}_{sur}^*$. Specifically, when $\Delta \dot{E}_{sur}^*$ exceeds a threshold around 0.038, which corresponds to a rapid conversion of kinetic energy into surface energy, a significant reduction in t_c^* can be achieved.

Based on our results, the following future endeavors can be extended to further enhance our understanding of the impinging dynamics of droplets. For example, due to constraints within the model, only a moderate density ratio of around 40 is examined. Future works may consider investigating other regimes in the density-ratio space. Additionally, this study is limited to regular array patterns, and only vertical droplet impingement is considered. One can potentially study the effect of oblique droplet impingement to introduce asymmetry in these processes.

ACKNOWLEDGMENTS

AUTHOR DECLARATIONS
Conflict of Interest

The authors have no conflicts to disclose.

Author Contributions

Xin Wang: Conceptualization (equal); Formal analysis (equal); Investigation (equal); Methodology (equal); Writing – original draft (equal); Writing – review & editing (equal). **Mengqi Zhang:** Conceptualization (equal); Formal analysis (equal); Supervision (equal); Writing – review & editing (equal). **Hui Tang:** Formal analysis (equal); Supervision (equal); Writing – review & editing (equal). **Chenglei Wang:** Conceptualization (equal); Funding acquisition (equal); Supervision (equal); Writing – original draft (equal); Writing – review & editing (equal).

DATA AVAILABILITY

The data that support the findings of this study are available from the corresponding author upon reasonable request.

REFERENCES

[1]A. L. Yarin, "Drop impact dynamics: Splashing, spreading, receding, bouncing," Annu. Rev. Fluid Mech. **38**, 159–192 (2006).
[2]D. Richard, C. Clanet, and D. Quéré, "Contact time of a bouncing drop," Nature **417**(6891), 811–811 (2002).
[3]T. M. Schutzius, S. Jung, T. Maitra, G. Graeber, M. Köhme, and D. Poulikakos, "Spontaneous droplet trampolining on rigid superhydrophobic surfaces," Nature **527**(7576), 82–85 (2015).
[4]S. Wildeman, C. W. Visser, C. Sun, and D. Lohse, "On the spreading of impacting drops," J. Fluid Mech. **805**, 636–655 (2016).
[5]X. Wang, B. Xu, S. Guo, Y. Zhao, and Z. Chen, "Droplet impacting dynamics: Recent progress and future aspects," Adv. Colloid Interface Sci. **317**, 102919 (2023).
[6]C. Qian, F. Zhou, T. Wang, Q. Li, D. Hu, X. Chen, and Z. Wang, "Pancake jumping of sessile droplets," Adv. Sci. **9**, 2103834 (2022).
[7]J. Hao, J. Lu, L. Lee, Z. Wu, G. Hu, and J. M. Floryan, "Droplet splashing on an inclined surface," Phys. Rev. Lett. **122**(5), 054501 (2019).
[8]D. Lohse, "Fundamental fluid dynamics challenges in inkjet printing," Annu. Rev. Fluid Mech. **54**, 349–382 (2022).
[9]S. Peppou-Chapman, J. K. Hong, A. Waterhouse, and C. Neto, "Life and death of liquid-infused surfaces: A review on the choice, analysis and fate of the infused liquid layer," Chem. Soc. Rev. **49**, 3688–3715 (2020).
[10]J. C. Bird, R. Dhiman, H. M. Kwon, and K. K. Varanasi, "Reducing the contact time of a bouncing drop," Nature **503**, 385–388 (2013).
[11]Y. Shen, J. Tao, H. Tao, S. Chen, L. Pan, and T. Wang, "Approaching the theoretical contact time of a bouncing droplet on the rational macrostructured superhydrophobic surfaces," Appl. Phys. Lett **107**, 111604 (2015).
[12]X. Chen, Y. Wang, Y. Yang, X. Wang, and D. J. Lee, "Contact time of droplet impact on superhydrophobic cylindrical surfaces with a ridge," Langmuir **39**(50), 18644–18653 (2023).
[13]L. Zhang, X. Chen, Y. Yang, and X. Wang, "Impact dynamics of a droplet on superhydrophobic cylinders structured with a macro ridge," Langmuir **39**(18), 6375–6386 (2023).
[14]S. Gao, J. J. Wei, B. Shi, S. Zheng, S. Yang, and Y. Wang, "X. Reducing the contact time of off-center impacts," Phys. Fluids **35**, 047113 (2023).
[15]Q. Tang, S. Xiang, S. Lin, Y. Jin, C. Antonini, and L. Chen, "Enhancing droplet rebound on superhydrophobic cones," Phys. Fluids **35**, 052101 (2023).
[16]H. Wang, H. Lu, and W. Zhao, "A review of droplet bouncing behaviors on superhydrophobic surfaces: Theory, methods, and applications," Phys. Fluids **35**, 021301 (2023).
[17]J. Lv, Y. Song, L. Jiang, and J. Wang, "Bio-inspired strategies for anti-icing," ACS Nano **8**(4), 3152–3169 (2014).
[18]Z. Hu, F. Chu, H. Shan, X. Wu, Z. Dong, and R. Wang, "Understanding and utilizing droplet impact on superhydrophobic surfaces: Phenomena, mechanisms, regulations, applications, and beyond," Adv. Mater. **36**, 2310177 (2024).
[19]Y. Liu, L. Moevius, X. Xu, T. Qian, J. M. Yeomans, and Z. Wang, "Pancake bouncing on superhydrophobic surfaces," Nat. Phys. **10**, 515–519 (2014).
[20]Y. Liu, G. Whyman, E. Bormashenko, C. Hao, and Z. Wang, "Controlling drop bouncing using surfaces with gradient features," Appl. Phys. Lett. **107**, 051604 (2015).
[21]L. Z. Wang, A. Zhou, J. Z. Zhou, L. Chen, and Y. S. Yu, "Droplet impact on pillar-arrayed non-wetting surfaces," Soft Matter **17**(24), 5932–5940 (2021).
[22]N. D. Patil, R. Bhardwaj, and A. Sharma, "Droplet impact dynamics on micro-pillared hydrophobic surfaces," Exp. Therm. Fluid Sci. **74**, 195–206 (2016).
[23]A. Hu and D. Liu, "3D simulation of micro droplet impact on the structured superhydrophobic surface," Int. J. Multiphase Flow **147**, 103887 (2022).
[24]J. Song, M. Gao, C. Zhao, Y. Lu, L. Huang, X. Liu, C. J. Carmalt, X. Deng, and I. P. Parkin, "Large-area fabrication of droplet pancake bouncing surface and control of bouncing state," ACS Nano **11**(9), 9259–9267 (2017).
[25]C. Wu, X. Qin, H. Zheng, Z. Xu, Y. Song, Y. Jin, H. Zhang, J. Mo, W. Li, J. Lu, and Z. Wang, "Self-adaptive droplet bouncing on a dual gradient surface," Small 2304635 (2023).
[26]Q. Ma, Y. Wang, Y. Wang, B. Zhang, S. Zheng, Y. Yang, D. Lee, and X. Wang, "Pancake bouncing of nanodroplets impacting superhydrophobic surfaces," Appl. Surf. Sci. **639**, 158273 (2023).
[27]A. M. Moqaddam, S. S. Chikatamarla, and I. V. Karlin, "Drops bouncing off macro-textured superhydrophobic surfaces," J. Fluid Mech. **824**, 866–885 (2017).
[28]S. Chen, H. Chen, D. Martnez, and W. Matthaeus, "Lattice Boltzmann model for simulation of magnetohydrodynamics," Phys. Rev. Lett. **67**(27), 3776 (1991).
[29]X. Wang, B. Xu, Y. Wang, and Z. Chen, "Directional migration of single droplet on multi-wetting gradient surface by 3D lattice Boltzmann method," Comput. Fluids **198**, 104392 (2020).
[30]A. L. Kupershtokh and D. A. Medvedev, "Lattice Boltzmann equation method in electrohydrodynamic problems," J. Electrostat. **64**(7–9), 581–585 (2006).
[31]A. L. Kupershtokh, D. I. Karpov, D. A. Medvedev, C. P. Stamatelatos, V. P. Charalambakos, E. C. Pyrgioti, and D. P. Agoris, "Stochastic models of partial discharge activity in solid and liquid dielectrics," IET Sci. Meas. Technol. **1**, 303–311 (2007).
[32]A. L. Kupershtokh, D. A. Medvedev, and D. I. Karpov, "On equations of state in a lattice Boltzmann method," Comput. Math. Appl. **58**, 965–974 (2009).

08 December 2025 09:23:46

[33]S. Gong and P. Cheng, "Numerical investigation of droplet motion and coalescence by an improved lattice Boltzmann model for phase transitions and multiphase flows," Comput. Fluids **53**, 93–104 (2012).

[34]X. Shan and H. Chen, "Simulation of nonideal gases and liquid-gas phase transitions by the lattice Boltzmann equation," Phys. Rev. E **49**(4), 2941 (1994).

[35]P. Yuan and L. Schaefer, "Equations of state in a lattice Boltzmann model," Phys. Fluids **18**(4), 042101 (2006).

[36]I. Ginzbourg and P. M. Adler, "Boundary flow condition analysis for the three-dimensional lattice Boltzmann model," J. Phys. II **4**, 191–214 (1994).

[37]Q. Li, K. H. Luo, Q. J. Kang, and Q. Chen, "Contact angles in the pseudopotential lattice Boltzmann modeling of wetting," Phys. Rev. E **90**(5), 053301 (2014).

[38]Z. Hu, F. Chu, and X. Wu, "Double-peak characteristic of droplet impact force on superhydrophobic surfaces," Extreme Mech. Lett. **52**, 101665 (2022).

[39]Z. Yin, R. Su, W. Zhang, Z. Ding, F. Chai, Q. Chen, Q. Wang, and F. Liu, "Oscillation characteristics of single droplet impacting vertically on smooth surfaces using volume of fluid method," Microgravity Sci. Technol. **33**(5), 58 (2021).

[40]X. Li, X. Ma, and Z. Lan, "Dynamic behavior of the water droplet impact on a textured hydrophobic/superhydrophobic surface: The effect of the remaining liquid film arising on the pillars' tops on the contact time," Langmuir **26**(7), 4831–4838 (2010).

[41]S. Gao, B. Wei, J. Jin, J. Ye, Y. Wang, S. Zheng, Y. Yang, and X. Wang, "Contact time of a droplet impacting hydrophobic surfaces," Phys. Fluids **34**(6), 067104 (2022).

[42]Y. Wang and S. Chen, "Droplets impact on textured surfaces: Mesoscopic simulation of spreading dynamics," Appl. Surf. Sci. **327**, 159–167 (2015).

[43]N. D. Patil, V. H. Gada, A. Sharma, and R. Bhardwaj, "On dual-grid level-set method for contact line modeling during impact of a droplet on hydrophobic and superhydrophobic surfaces," Int. J. Multiphase Flow **81**, 54–66 (2016).

[44]J. Li and P. B. Weisensee, "Low Weber number droplet impact on heated hydrophobic surfaces," Exp. Therm. Fluid Sci. **130**, 110503 (2022).

08 December 2025 09:23:46